

# Characterization Techniques for a MEMS Electric-Field Sensor in Vacuum

Simon Ghionea

Sensors and Electron Devices Directorate

U.S. Army Research Laboratory

phone: (1) 301-394-1844

e-mail: simon.j.ghionea.civ@mail.mil

David Hull

Sensors and Electron Devices Directorate

U.S. Army Research Laboratory

phone: (1) 301-394-3140

e-mail: david.m.hull6.civ@mail.mil

*Abstract*— An accurate calibration of an electric-field sensor is difficult to carry out due to challenges involved in generating a uniform electric field over the sensor volume. Additionally, capacitive coupling between the field source and the sensors and related instrumentation tends to distort the measured field further. Sensor characterization includes not only calibration, but also determination of the frequency response (both magnitude and phase), noise power spectral density, dynamic range, and linearity. In this paper, we discuss characterization techniques for an unpackaged microelectromechanical systems (MEMS) electric field sensor in a vacuum chamber. The use of oppositely charged square plates at a spacing of half the plate width is advised by the IEEE 1308-1994 standard for generation of a uniform electric field. Previously, the U.S. Army Research Laboratory (ARL) has shown that by employing guard tubes in the construction of an electric field generating chamber, the fringing fields can be controlled, and the spacing between the endplates can be increased while maintaining a uniform field. A similar, smaller apparatus for generating a uniform axial electric field was constructed to fit into a vacuum bell jar. The considerations and techniques for minimizing error due to fringing and distortion from metal conductors will be presented, along with the techniques and laboratory equipment used for characterizing the sensor.

## I. INTRODUCTION

There are a number of microelectromechanical systems (MEMS)-based electric-field sensors (EFS) that have been reported in the literature. The majority of the reported sensors are based on the field-mill principle with MEMS-actuated electrodes [1–11]. These sensor types, when actuated at their mechanical resonant frequencies, operate optimally in a vacuum environment to increase the resonator quality factor due to the absence of air damping effects. To support the research and development phase of new EFS requiring operation under vacuum, it is important to be able to characterize their sensor response without the complexities associated with vacuum packaging. ARL has previously shown that the accuracy of the generated electric field by an electric-field generator may be increased by employing guard tubes around the perimeter [12–13]. This concept is employed in the construction of an electric-field generator inside a vacuum system. The current work presents a system that was built to test, measure, and characterize an unpackaged, new, and unique MEMS electric-field sensor that requires a vacuum environment.

## II. SENSOR PRINCIPLE OF OPERATION

The sensor, referred to as a steered-electron electric-field sensor (SEEF sensor), is depicted in operation in Fig. 1. Current flows through a micromachined tungsten cathode filament, resulting in thermionic electron emission due to heating. A low work-function coating on the tungsten keeps the operating temperature at around 1200 K. Some electrodes (not shown) biased a few volts above the cathode potential act as a gate, controlling the electron current that flows upwards. Two electrodes at a distance of 2 mm away serve as the anodes, and collect the current flowing upwards out of the cathode. Without an external applied electric field, the electron currents collected at Anode 1 and Anode 2 are approximately equal. With an applied electric field perpendicular to the sheet of electrons, the negatively-charged electrons are attracted to the source of the field through Coulomb's law and they are deflected slightly as they traverse the gap on their way to the anode electrons. As a result, the electron current to Anode 1 decreases while the current to Anode 2 increases by the same amount. The difference between the two anode currents is the transducer's measured quantity, and is proportional to the applied perpendicular electric field.

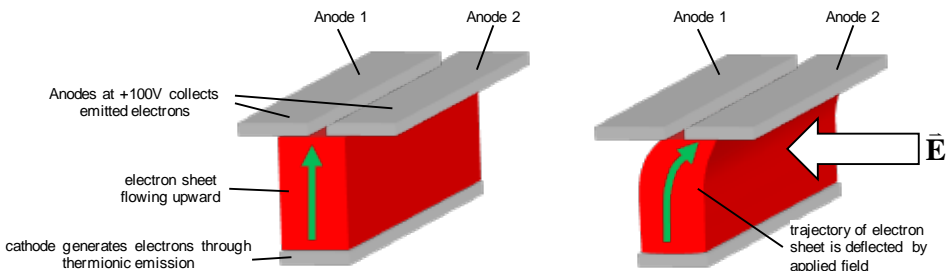


Fig. 1 Illustration of the concept of operation for the Steered-electron electric-field (SEEF) sensor.

The cathode must operate under high vacuum to avoid oxidizing, and so that electrons do not collide with air molecules. Since the sensor is undergoing active research and development with several design iterations that must be tested, vacuum packaging is a more complicated and expensive process that will un-necessarily complicate development during initial phases, hence the need for the vacuum electric-field characterization system. As seen in Fig. 2, the SEEF sensor is assembled from a glass cathode chip on the bottom, a 2-mm-thick glass spacer chip in the middle, and a glass anode chip on the top. The anode chip has the pair of anodes on the bottom and bond pads on the top. The anode

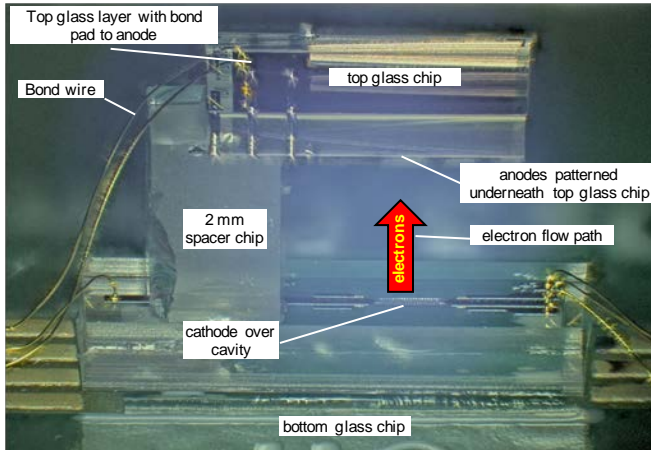


Fig. 2 Photograph showing stack of three glass chips mounted on a printed-circuit board: cathode chip on the bottom, spacer chip in the middle, and anode chip on the top.

### III. ELECTRIC FIELD GENERATORS

The goal of an electric-field generator is to generate a known electric field with a high degree of spatial uniformity over a working volume, to be used for calibration and characterization of EFS. Only quasi-static fields are of interest to this sensor application. In this regime of low frequencies (typically less than 100 kHz), the magnetic and the electric field are approximated to be uncoupled. The standard method of generating an electric field is through the use of parallel conducting plates of separation distance  $d$  held at a potential difference  $V$ . When the plates are of infinite size, the field everywhere between the plates is given by

$$E = V/d \quad (V/m) . \quad (1)$$

For plates that are of finite size, the actual field differs from Eq. 1 due to the effects of fringing. The fringing extends all the way to the center, but it is minimized there. The IEEE Standard 1308 electric-field generator illustrated in Fig. 3(a), suggests using square parallel plates, which are spaced at half of the length of the plate edge [14]. Fringing errors are not controlled in this scheme; however, the standard indicates that by using the suggested dimensions, the uniform area is maximized in the center. A major disadvantage is the relatively small separation between plates, which can lead to capacitive coupling effects between a device under test in the center and at the end plates.

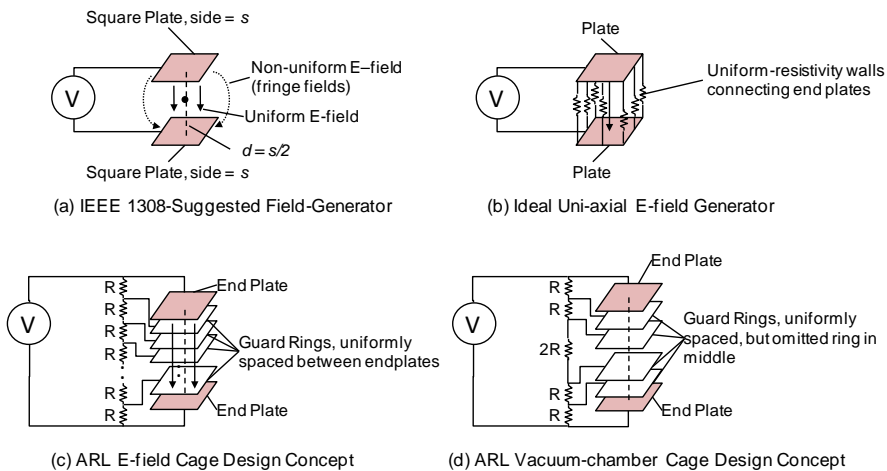


Fig. 3 Shown are diagrams of various electric-field generator schemes.

Fig. 3(b) presents an ideal quasi-static uniaxial E-field generator, where the endplates are surrounded by uniform-resistivity walls. Current flowing along the walls produces a linearly graded fall of potential along the walls, creating planes of constant voltage through the inside volume. IEEE Standard 644 suggests a more practical scheme as shown in Fig. 3(c) [15]. ARL has constructed a room-sized electric-field generator based on this principle, which can generate uniaxial electric fields with high accuracy and uniformity over more than  $1 \text{ m}^3$  volume [12-13].

The available bell jar vacuum chamber volume (Fig. 4) is a mechanical constraint that must be worked around. The limited space available in a vacuum bell jar makes the E-field generation scheme presented in Fig. 3(a) appealing. However, small spacing between the plates leads to a capacitive coupling effect, and the uniform field volume is limited. Thus, it was decided to use a method shown in Fig. 3(d), which is based on the room-sized ARL E-field cage (Fig. 3(c)).

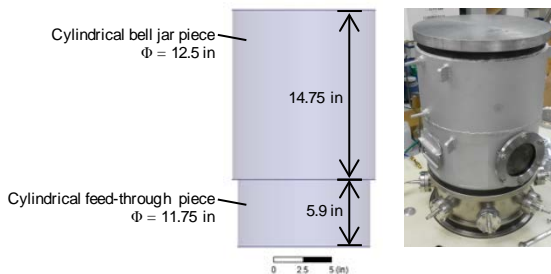


Fig. 4 Drawing and photo of vacuum system outfitted for E-field sensor testing.

#### IV. DESIGN OF VACUUM E-FIELD GENERATOR

Fig. 3(d) presents a scheme where guard rings are used as in Fig. 3(c), but there are rings in the center that are removed/omitted. The resistors in the resistor divider are iden-

tical, with the exception of the resistor spanning the gap, which must be an integer multiple depending on how many rings are missing from the middle. When a voltage is applied to the endplates, the current flow in the series resistor circuit should generate a linear fall of potential across the rings as a function of position. Fig. 3(d) is preferred for the vacuum chamber testing over Fig. 3(c) because the omission of the ring tubes in the center allows for sample removal/insertion, as well as convenient routing of drive and signal wires. A diagram showing the vacuum cage concept, as compared to a standard parallel plate cage, is shown in Fig. 5. The design approach and concepts will now be discussed.

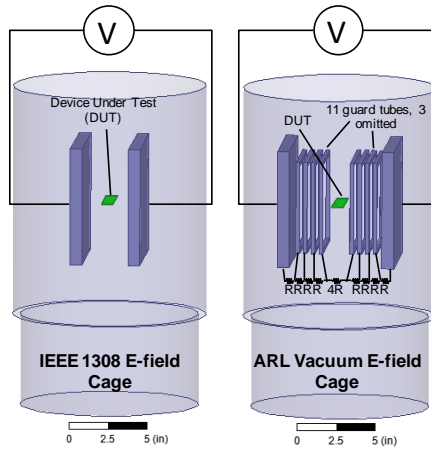


Fig. 5 Diagram showing comparison of ARL Vacuum E-field cage to a standard parallel plate arrangement per IEEE 1308.

An aluminum vacuum bell jar with dimensions as in Fig. 4 was used. This bell jar acts as a Faraday shield that surrounds the electric-field generator cage. Extensive modeling and simulation was performed using an in-house Method of Moments modeling software. In these models, a grounded conducting sphere was positioned in the center of the cage, representing the region of interest (ROI) enclosed within that sphere's volume. Using this technique, the error can be easily quantified within the volume because the electric-field on a sphere in a uniaxial ambient field is an exact solution. This gives a worst-case error for an object represented by the dimensions of the sphere in the model. For the design constraints, square end-plates of 5.9 in and 0.25 in thickness were used due to the available vacuum chamber bell jar dimensions. A length of 6.0 in (inside end-plate to inside end-plate) was chosen to comfortably fit inside the chamber. The guard-rings are made square in perimeter (like the end-plates), as well as cross-sectional area. It has been previously shown that the spacing between rings must not be large compared to the cross-guard ring sectional area [16].

A variety of 3D Method-of-Moments models were generated and analyzed. Guard rings with square cross-sections of 0.25 in were selected based on modeling. Fig. 6 shows the percent error (deviation from the theoretical ideal field from Eq. 1) for several arrangements of an E-field cage. The more guard rings employed in the design, the lower the error in the resulting error in the E-field and the higher uniformity. Models were also simulated for a configuration where there were five guard rings, but one was omitted from the center. One significant result is the minimal difference between the fields due to

five guard rings and five guard rings with the center ring omitted. This is explained because the majority of the error introduced into the entire field structure is caused by errors close to the end plates, not by errors introduced due to perturbations occurring near the center. This modeling shows verification of the concept in Fig. 5(d).

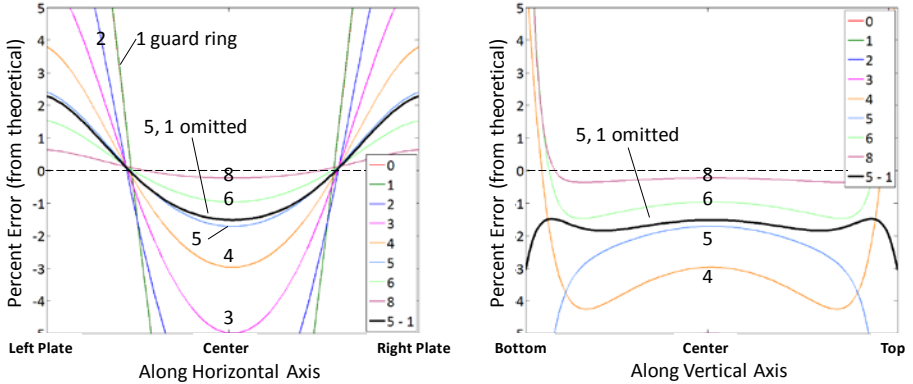


Fig. 6 Percent of E-field error comparing varying amount of guard rings, as well as a configuration where there is one guard ring omitted from the center. The inside spacing between endplates is 6.0" and the endplates are 5.9" on an edge and 1/2" thickness. The guard rings are spaced equi-distant between the endplates, and the omitted guard rings are missing from the center. The cage is enclosed in a faraday shield.

To further study the effect of omitting guard rings, Fig. 7 shows the error contained in the fields inside a spherical ROI for several configurations of the guard tubes. For emphasis, an E-field generator with no guard tubes (and close spacing, similar to what would be suggested by IEEE 1308) is also shown on the plot. The 11-3 configuration gives excellent results for a spherical ROI up to 1 inch in diameter.

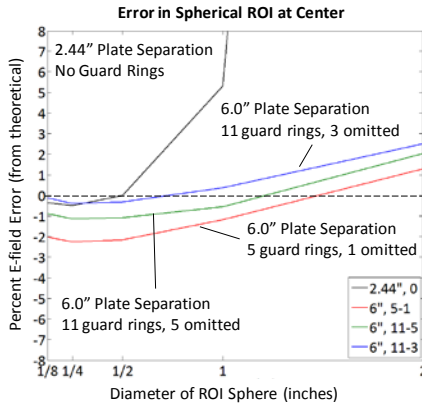


Fig. 7 Percent of E-field error within a spherical ROI for various ROI diameters and cage configurations. The endplates are 5.9" on an edge and 1/2" thickness. The guard rings are spaced equi-distant between the endplates, and the omitted guard rings are missing from the center.

## V. REALIZED VACUUM E-FIELD GENERATOR SYSTEM

Based on the analysis of the various method-of-moments simulations in the preceding section, a finalized E-field generator design was selected with a square plate of 5.9 in, 11 guard rings with three omitted from the center, guard rings with cross-section area of 0.25 in, and an inside plate separation of 6 in. Note that 11 tubes create 12 spaces, which implies 0.5 in per space. The distance between the inside of the endplate and the center of the first guard tube is 0.5 in. The (air) space between adjacent tubes is 0.25 in (0.50 in – 0.25 in), while the (air) space between the center two tubes is 1.75 in ( $4 \times 0.50$  in – 0.25 in).

For the final E-field generator mechanical design, additional elements were added to support sensor measurement tests: a center shielding post to shield signal wires from the generated E-field, as well as offer mechanical support for the sample holder; and side tubes to shield drive wires and a bottom shielding plate. The final realized design is shown in Fig. 8. For connections between the uniformly spaced endplates, 255- $\Omega$  resistors were used. For the gap where three guard rings are omitted, a resistor of 1020  $\Omega$  was used. This gives a total resistance of 3.06 k $\Omega$ . This load is high enough that it may be driven by a 50- $\Omega$  source function generator, and low enough that the distortion due to RC effects at frequencies up to tens of kHz is not compromised.

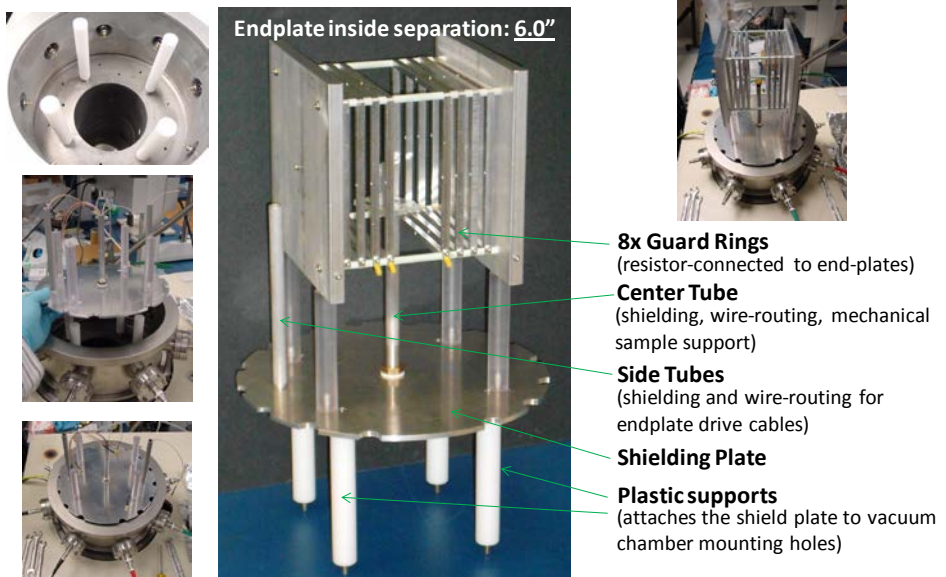


Fig. 8 Photos of E-field generator installed in vacuum system, with bell-jar cover removed

To verify the electric-field generator performance, the voltages on each of the guard rings and endplates are measured differentially using an automated testing system. The end plates are driven with a dual-channel function generator, configured to drive one plate at 180° out of phase to the other plate. This creates a virtual AC ground in the center plane of the cage. For two frequencies, the voltages of the plates and guard ring versus distance are plotted in Fig. 9(a). The potential falls linearly with position. For an understanding of the frequency response and a calculation of the resistor mismatches, the mag-

nitude and phase of the differential voltage across each resistor is measured, and compared to the theoretical magnitude based on the resistor-divider network in Fig. 9(b). At frequencies below 20 kHz, the resistors are matched better than within 0.1%. Above 20 kHz, parasitic effects of the system begin to manifest. However, even at 50 kHz the error is less than 1%. At 100 kHz, the voltage error is less than 3% due to the parasitics.

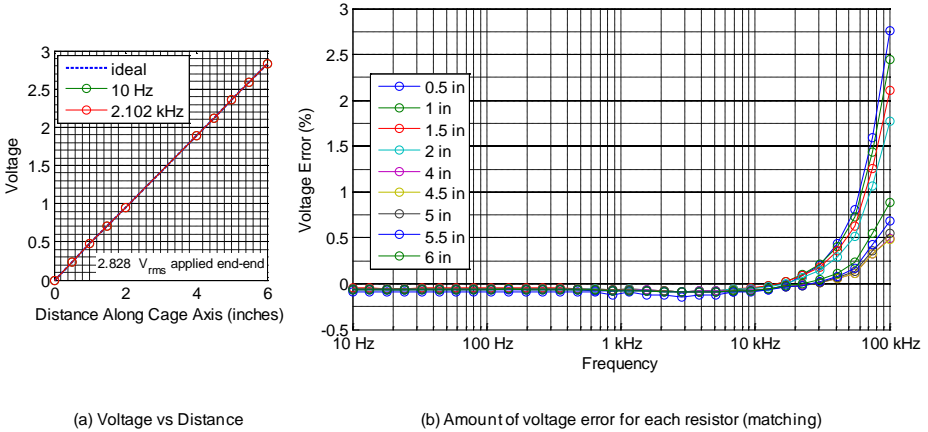


Fig. 9 Electric-field cage performance measurements. (a) Voltage vs distance (b) Voltage percent error for each resistor. This indicates resistor value mismatches. At high frequencies, inductive parasitic effects in the system begin to dominate. The voltage error is less than 0.1% at frequencies below 50 kHz.

## VI. CHARACTERIZATION OF MEMS SENSORS IN VACUUM

Several characterization measurements are possible in the constructed apparatus. Measurements of frequency response are made by sweeping the frequency of the voltage applied across the endplates of the E-field generator. Linearity is obtained by sweeping the E-field amplitude. For noise measurements, the endplates are held at zero applied voltage, using the aluminum vacuum chamber bell jar as a good Faraday enclosure to screen out stray E-fields. Finally, from the above measurements, it is possible to determine the limit of detection. An automated testing system based on phase sensitive detection was built and constructed to carry out the previous measurements on each device. Many SEEF devices were measured, but only representative results are included in this paper. A thorough discussion of the devices tested is beyond the scope of this paper.

A measurement of sensitivity and frequency response is shown in Fig. 10. The plot on the left shows amplitude magnitude data in units of volts. Each trace corresponds to a frequency sweep using a particular applied field amplitude. The lines for 0.0182, 0.181, 1.8, 17.9, and 178.4  $V_{rms}/m$  appear to follow the same frequency response. Thus, 17.9  $V/m$  was chosen to form a linear calibration and translate the data into units of transduced field ( $V/m$ ). At high fields, the device exhibits greater gain above about 1 kHz: this non-linearity can be seen in the data for 178.4  $V/m$ . This non-linear performance may limit the effective dynamic range for some applications. At low fields, the device noise will also limit the dynamic range: this can be seen in the 18.2  $mV/m$  field measurement. Figure 8b shows that the device has good (corrected) linearity over a 40-dB dynamic range,

and relatively poor linearity (or a lower frequency response) over almost 80 dB of dynamic range.

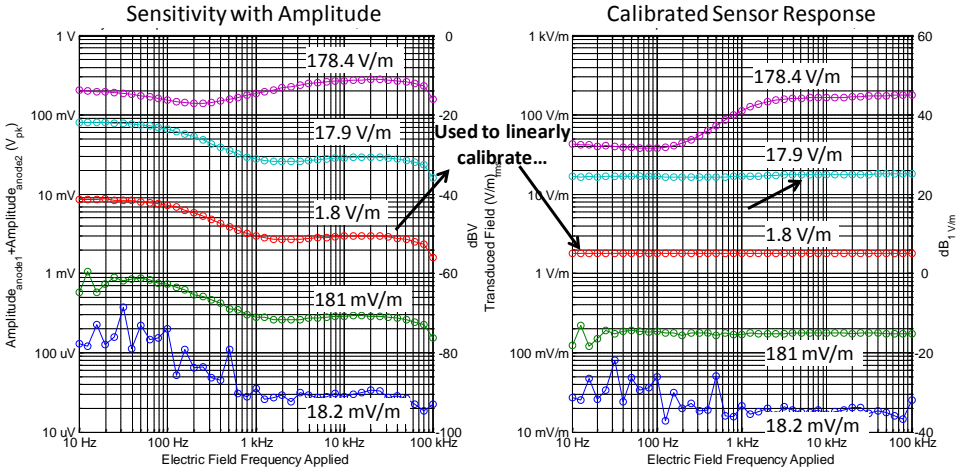


Fig. 10 The device frequency response was measured using various amplitudes for the applied field. One curve (1.8  $V_{rms}/m$ ) is selected as the calibration to translate the sensor response to transduced units of  $V_{rms}/m$  measured, for a particular  $V_{rms}/m$  applied.

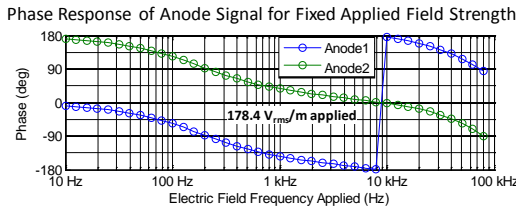


Fig. 11 Phase response of Anode 1 and Anode 2 signals taken individually. The phase indicates the deviation from the phase of applied electric field. A fixed field strength was used.

The phase response from the current collected at each of the anodes in the SEEF sensor is shown in Fig. 11 for a fixed applied field strength. The relative phase difference between the two anodes is approximately  $180^\circ$ , which confirms proper electron-beam deflection in the SEEF sensor in response to an applied electric-field. There is a frequency-dependence in the phase response of the sensor to an applied field.

Noise spectral density measurements were obtained by doing time-domain sampling of the sensor outputs for 20 seconds. Measurements were also taken without the sensor connected so that the noise contributions of the transimpedance amplifier and the digitizer may be determined. The raw voltage data, after processing with an FFT with 50 mHz frequency bins, is plotted in  $V_{rms}/\sqrt{rtHz}$  in Fig. 11 (left). The linear calibration obtained in the Fig. 10 data may be applied to Fig. 11 (left) to finally determine a fundamental limit of detection at each frequency point in the spectrum, shown in Fig. 11 (right). It is important to note that the limit of detection of the sensor in Fig. 11 (right) assumes a signal-to-noise ratio (SNR) of 1. A sensed field of 18.2 mV/m is below the noise power spectral

density line at low frequencies, but above the noise at higher frequencies. This reinforces the data in Fig. 10.

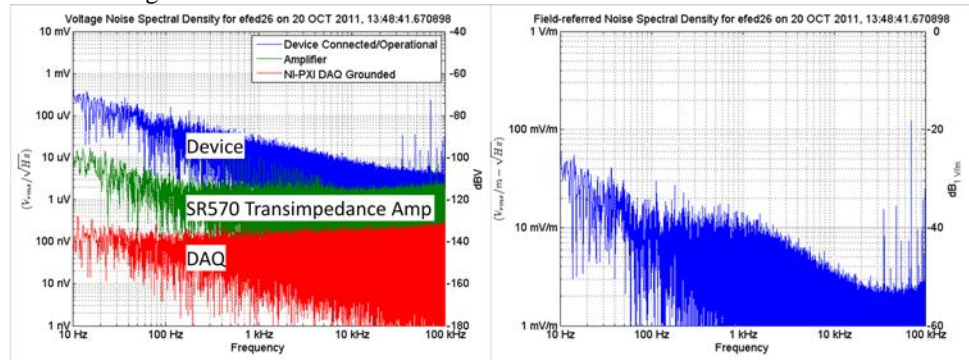


Fig. 12 (left) Noise spectral density in terms of  $V_{rms}/\text{rtHz}$ . The noise may be seen in terms of the device transduction physics, signal conditioning (transimpedance amp), and DAQ. (right) Field-referred noise spectral density in terms of  $(V_{rms}/\text{m})/\text{rtHz}$ . The limits of detection read off the plot assume an SNR of 1.

## VII. CONCLUSION

As research progresses in the area of MEMS E-field sensors, some devices will operate optimally under a vacuum environment. This paper has presented a testing system that may be used in the research and development process for such novel E-field sensors to quickly obtain sensor characterization measurements prior to expensive vacuum packaging. In an iterative design-process, more sensor concepts can be fabricated and subsequently measured in a shorter period of time.

The testing system described in this paper uses a variant of the ARL E-field cage, with guard tubes to create the largest and most uniform electric fields in a vacuum chamber. A phase-sensitive source and detection electronics are used to measure frequency response, noise power spectral density, linearity, and dynamic range. Examples of each of these measurements are provided in this paper.

## VIII. ACKNOWLEDGEMENTS

Dr. Kirt Williams is the EFED program lead from SAIC and his team designed and fabricated the SEEF sensor. Ross Adelman carried out extensive simulations and analysis of the electric-field generator configurations, which aided in the design of the final apparatus. Dr. Matthew Ervin assembled the vacuum chamber hardware setup and provided support.

## REFERENCES

- [1] M.N. Horenstein et al., "A micro-aperture electrostatic field mill based on MEMS technology," *Journal of Electrostatics*, vol. 51-52, pp. 515–521, 2001.
- [2] P.S. Riehl et al., "Electrostatic charge and field sensors based on micromechanical resonators," *Microelectromechanical Systems, Journal of*, vol. 12, no. 5, pp. 577–589, 2003.
- [3] C. Gong et al., "Electric field sensors based on MEMS technology," *J. of Electron.(China)*, vol. 22, no. 4, pp. 443–448, 2005.

- [4] A. Roncin et al., "Electric field sensor using electrostatic force deflection of a micro-spring supported membrane," *Sensors and Actuators A: Physical*, vol. 123-124, pp. 179–184, 2005.
- [5] X. Chen et al., "Thermally driven micro-electrostatic fieldmeter," *Sensors and Actuators A: Physical*, vol. 132, no. 2, pp. 677–682, 2006.
- [6] C. Peng et al., "A Novel High Performance Micromechanical Resonant Electrostatic Field Sensor Used In Atmospheric Electric Field Detection," *Micro Electro Mechanical Systems, 2006. MEMS 2006 Istanbul. 19th IEEE International Conference on*, 2006, pp. 698–701.
- [7] T. Denison et al., "A Self-Resonant MEMS-based Electrostatic Field Sensor with 4V/m/Hz Sensitivity," *Solid-State Circuits Conference, 2006. ISSCC 2006. Digest of Technical Papers. IEEE International*, 2006, pp. 1121–1130.
- [8] B. Bahreyni et al., "Design and Testing of a Field-Chopping Electric Field Sensor using Thermal Actuators with Mechanically Amplified Response," *Solid-State Sensors, Actuators and Microsystems Conference, 2007. TRANSDUCERS 2007. International*, 2007, pp. 1397–1400.
- [9] G. Wijeweera et al., "Measuring power system voltage remotely using micromachined electric field sensor," *Microsystems and Nanoelectronics Research Conference, 2008. MNRC 2008. 1st*, 2008, pp. 209–212.
- [10] C. Peng et al., "Design of a novel closed-loop SOI MEMS resonant electrostatic field sensor," *Procedia Engineering*, vol. 5, pp. 1482–1485, 2010.
- [11] C. Peng et al., "Detecting internal defect of non-ceramic insulators using a novel micromachined electric field sensor," *Micro Electro Mechanical Systems (MEMS), 2011 IEEE 24th International Conference on*, 2011, pp. 561–564.
- [12] D.M. Hull et al., "ARL Electric-field Cage Modeling, and Design," *Proc. ESA/IEJ/IEEE-IAS/SFE Joint Conference on Electrostatics 2006*, 2006, pp. 148–157.
- [13] D.M. Hull et al., "ARL Electric-field Cage Modeling, Design and Calibration," *Electromagnetic Field Computation, 12th Biennial IEEE Conference on*, Miami, FL: 2006, p. 89.
- [14] "IEEE recommended practice for instrumentation: specifications for magnetic flux density and electric field strength meters-10 Hz to 3 kHz," *IEEE Std 1308-1994*, 1995.
- [15] "IEEE standard procedures for measurement of power frequency electric and magnetic fields from AC power lines," *IEEE Std 644-1994*, 1995.
- [16] D.M. Hull et al., "Systems and methods involving electric-field cages," U.S. Patent 7529075, May 5, 2009.